CrossMark

Three-dimensional graphene frameworks wrapped $Li_3V_2(PO_4)_3$ with reversible topotactic sodium-ion storage

Fangyu Xiong, Shuangshuang Tan, Qiulong Wei, Guobin Zhang, Jinzhi Sheng, Qinyou An*, Liqiang Mai*

State Key Laboratory of Advanced Technology for Materials Synthesis and Processing, Wuhan University of Technology, Wuhan 430070, PR China

ARTICLE INFO

ABSTRACT

$Li_3V_2(PO_4)_3$ (LVP) was evaluated as a promising cathode material for sodium-ion batteries (SIBs). The three-dimensional graphene frameworks wrapped LVP (LVP-G-FD) exhibited high energy density of 501.3 Wh kg^{-1}, which is almost the highest energy density among the known polyanionic cathodes for SIBs. The enhanced electrochemical performance of LVP-G-FD is attributed to the graphene framework which provides the fast electronic transport network and buffering space. Besides, the sodium-ion storage mechanism of LVP was investigated *via in-situ* XRD and so on. The sodium-ion storage process is composed of the electrochemical topotactic replacement and the subsequent topotactic reaction.

1. Introduction

The establishment of low-cost and efficient energy storage systems (ESSs) is necessary for the application of renewable energy [1–3]. Although lithium-ion batteries (LIBs) have been widely used in the portable electronics and extended to electric vehicles and hybrid electric vehicles due to its various advantages, the limited reserve and rising price restrict its application in large-scale ESSs [3–6]. Thus, the search for the substitutions of LIBs has attracted great attention from many researchers. Sodium-ion batteries (SIBs) have been investigated as the replacement for LIBs due to the similar electrochemical intercalation behavior between lithium-ion and sodium-ion [3–5,7]. Moreover, the low-cost and abundance of sodium compounds make SIBs hold high promise for application in large ESSs. However, the larger ionic radius (0.98 Å *vs.* 0.69 Å for lithium ion) requires the larger tunnel and space in electrode materials, hence obtaining suitable electrode materials for SIBs still remains a challenge [3,8].

Recently, many materials, including metal oxides (such as Na_xMO_2 (M=Co, Mn, Ni) [9–11], V_2O_5 [12], $V_2O_5 \cdot nH_2O$ [13], MoO_3 [14] and polyanionic compounds (such as $Na_3V_2(PO_4)_3$ (NVP) [8,15], $Na_2MP_2O_7$ (M=Fe, Co, Mn) [16–18] and $NaFe(SO_4)_2$ [19]), have been investigated as cathode for SIBs. Compared to metal oxides, polyanionic compounds usually exhibit better thermal and structural stability, which is favorable to realize better safety and longer cycle life [15,20,21]. Among the polyanionic compounds, NVP has been considered as one of the most promising cathode materials for SIBs due to

its NASICON (Na$^+$ ion superionic conductor)-related crystal structure with large ion channel and fast Na$^+$ ion diffusion coefficient, resulting in the stable Na$^+$ ion insertion and extraction [15,22–24]. However, the limited capacity (theoretical capacity of 118 mAh g^{-1}) and the medium potential (~3.4 V) of NVP lead to the low energy density (~400 Wh kg^{-1}), which is difficult to be comparable with those of most cathode materials for LIBs [15,23,24]. Therefore, the exploitation of high energy density cathode materials is of great significance for the development of SIBs. Compared to NVP, monoclinic $Li_3V_2(PO_4)_3$ (LVP), another NASICON-related compound, exhibits higher potential and higher capacity of lithium-ion insertion/extraction which means higher energy density [22,25]. If the LVP can be used as cathode materials for SIBs after being modified, it will hold high promise to improve the energy density of SIBs and promote the development of SIBs.

Herein, we realize the reversible sodium-ion insertion/extraction in lithium ion sites of LVP *via* an electrochemical topotactic replacement method. To the best of our knowledge, it may be the first time to use LVP as cathode material for SIBs. Considering the poor electronic conductivity of LVP which electrochemical performance of LVP, the graphene has been introduced to modify LVP [20,25]. The modified LVP (graphene framework wrapped LVP, denote as LVP-G-FD) achieves a high energy density about 501.3 Wh kg^{-1} (a discharge capacity of 147 mAh g^{-1} with average discharge voltage of 3.41 V). The graphene framework provides the efficient electronic conduction network and buffering space for the LVP nanoparticle, playing an

---
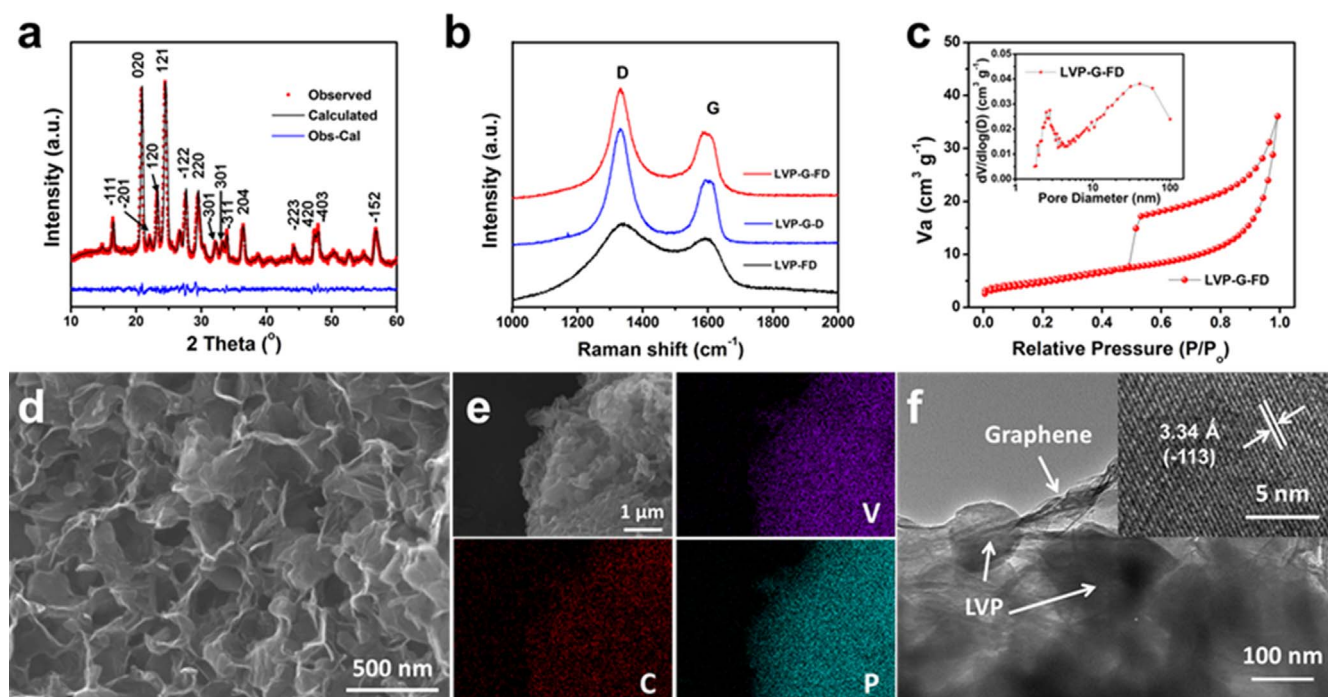
Fig. 1. (a) XRD pattern of LVP-G-FD with Rietveld refinement; (b) Raman spectra of LVP-G-FD, LVP-G-D and LVP-FD. (c) Nitrogen adsorption-desorption isotherms and corresponding pore size distribution (insert) of LVP-G-FD. (d) FESEM image, (e) EDS elemental mappings, (f) TEM image and HRTEM image (inset) of LVP-G-FD.

important role in the improvement for capacity, rate performance and cycling stability of LVP [26–31]. Besides, the ion insertion/extraction mechanism of LVP as cathode for SIBs has been investigated *via in-situ* X-ray diffraction (XRD) and inductively coupled plasma (ICP) technology.

2. Results and discussions

The crystal structure of LVP-G-FD has been investigated by XRD (Fig. 1a). According to the Rietveld refinement, all the diffraction peaks of LVP-G-FD can be readily indexed to monoclinic LVP. No impurity can be detected, confirming the high phase purity of LVP-G-FD. In addition, the refined lattice parameters are displayed in Table S1. Besides, the similar results were analyzed from the XRD patterns of LVP-G-D (the sample replaced freeze-drying treatment by direct drying) and LVP-FD (the sample without adding graphene) (Fig. S1). The Raman spectrum of LVP-G-FD is shown in Fig. 1b. Two intense bands located at 1260–1400 and 1540–1650 cm^{-1} are assigned to the D-band (disorders or defects) and G-band (graphite), respectively, demonstrating the existence of carbonaceous materials [32,33]. Based on the elemental analysis, the carbon contents of LVP-G-FD, LVP-G-D and LVP-FD are 4.4%, 4.6% and 0.6%, respectively. The carbon in LVP-FD is attributed to the carbonization of CH_3COO^- and $C_2O_4^{2-}$ anions during annealing process [22].

The pore structure and Brurauer-Emmerr-Teller (BET) specific surface area of the three samples were investigated with nitrogen isothermal-adsorption technology. The isotherm of LVP-G-FD appears to be a type II curve with H3 hysteresis loop (Fig. 1c). The BET surface area of LVP-G-FD is estimated to be 17.9 $m^2 \, g^{-1}$ and larger than those of LVP-G-D (8.5 $m^2 \, g^{-1}$) and LVP-FD (9.0 $m^2 \, g^{-1}$), indicating that a larger contact area between electrode and electrolyte may be obtained. The pore-size distribution curve (inset of Fig. 1c) displays that the pore sizes of LVP-G-FD are mainly 2–4 nm and 20–80 nm. LVP-G-D possesses similar pore-size distribution while LVP-FD displays a wide distribution (Fig. S2).

The morphology of the as-synthesized samples has been characterized *via* field emission scanning electron microscopy (FESEM) and

transmission electron microscopy (TEM). The sizes of LVP-G-FD blocks are several micrometers with rough surface (Fig. S3). The FESEM images of the fracture surface for LVP-G-FD blocks (Fig. 1d and Fig. S3d) show the block is composed of the graphene frameworks and LVP nanoparticles with size about 100–200 nm. In the FESEM images of LVP-G-D (Fig. S4a, b), graphene sheets are obvious in the composite but the graphene framework are not observed, indicating the freeze-drying treatment is necessary for the generation of graphene framework. The LVP-FD is composed of particles with size about several hundred nanometers, which are bigger than nanoparticles in LVP-G-FD and LVP-G-D, implying that the introduction of graphene decreases the size of particles by restraining their growth (Fig. S4c, d). In addition, the energy dispersive spectrometry (EDS) elemental mappings show that the V, P, and C elements are homogeneously distributed in LVP-G-FD (Fig. 1e). The TEM images (Fig. 1f and Fig. S5) of LVP-G-FD further demonstrate that the nanoparticles are wrapped in the graphene framework with void space between nanoparticles. The nanoparticles and graphene nanosheets are also observed in the TEM image (Fig. S6) of LVP-G-D, but the graphene nanosheets are dispersive and partly separate from LVP nanoparticles. The high resolution TEM (HRTEM) image (inset of Fig. 1f) of LVP-G-FD displays the lattice distance of 3.34 Å, corresponding to the *d*-space of (−113) planes in monoclinic LVP.

The coin cells with metallic sodium as anode have been assembled to investigate the electrochemical performance of LVP. First, LVP-G-FD cathode was measured at potential range from 2.5 to 4.5 V. A high initial discharge capacity of 147 mAh g^{-1} (based on the mass of LVP) with average discharge potential of 3.41 V was obtained at the current density of 20 mA g^{-1} (Fig. 2a). The charge/discharge curves of LVP-G-FD are similar to that of LVP as cathode for LIBs with three Li^+ ions insertion/extraction per formula [25]. In order to investigate the influence of Li^+ ions on the capacity, LVP-G-FD was first charged to extract lithium-ions and discharged after replacing the electrolyte containing lithium-ions by new SIBs electrolyte. A similar discharge capacity (148 mAh g^{-1}) was obtained at the same current density (Fig. S7), indicating that the influence of Li^+ ions is negligible. Thus, the subsequent measurement of electrochemical performance was carried
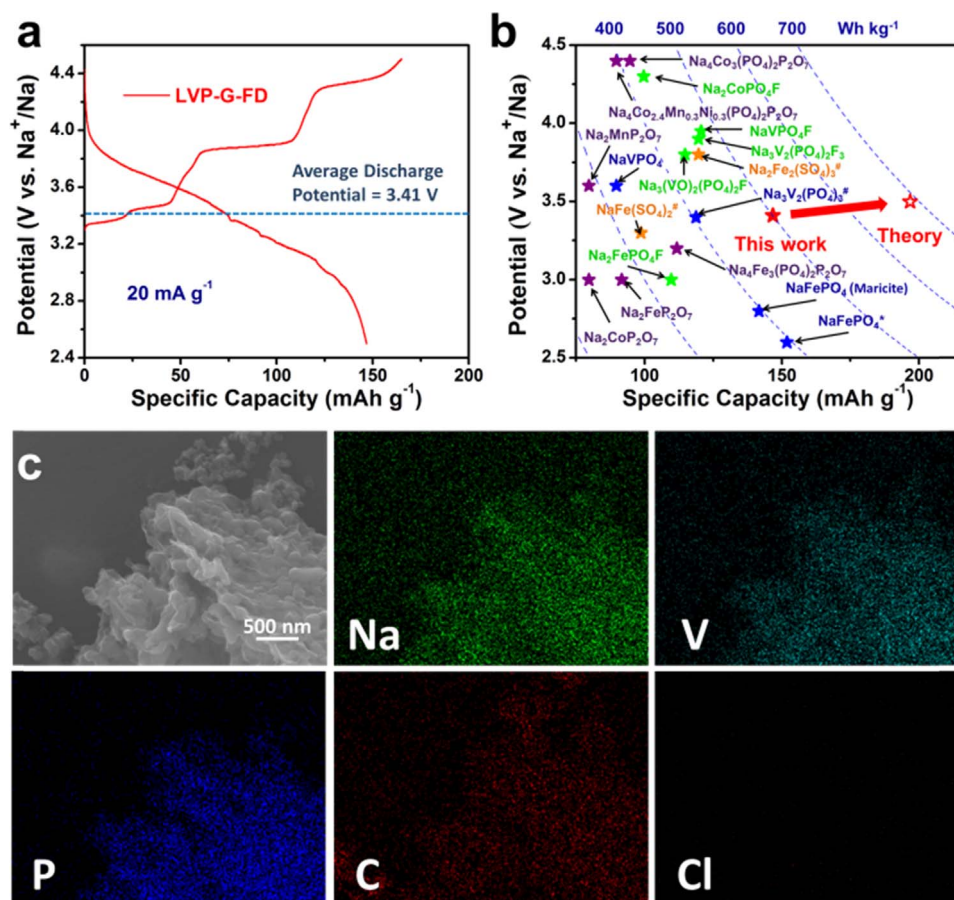
Fig. 2. (a) Charge/discharge curve of LVP-G-FD at the first cycle in the potential window of 2.5–4.5 V (the specific capacity based on the mass of LVP). (b) Comparison of the main polyanionic cathode materials for SIBs (*synthesis from LiFePO₄ *via* ion exchange, # based on the theoretical capacity) [16–19,34–46]. (c) The EDS elemental mappings of LVP-G-FD after first cycle in the potential window of 2.5–4.5 V.

out without replacing the electrolyte. The calculated energy density is about 501.3 Wh kg^{-1}, which is almost the highest energy density among the known polyanionic cathodes for SIBs (Fig. 2b) [16–19,34–46]. Moreover, further optimizing to reach theoretical capacity (197 mAh g^{-1}) can achieve energy density of > 650 Wh kg^{-1}. The EDS mappings of LVP-G-FD after first cycle are shown in the Fig. 2c. The electrolyte in the LVP-G-FD cathode was removed by repeatedly washing with alcohol. The content of Cl elements is few and the existence of Na element is obvious, indicating the insertion of sodium-ion during the first cycle. However, the capacity decreases to 98 mAh g^{-1} after 20 cycles, corresponding to a low retention (Fig. S8). According to the report for LVP as LIBs cathode, the insertion/extraction of third ion in LVP would lead to larger change of crystal structure, which restrained the cycling stability [47]. Thus, a potential range from 2.5 to 4.2 V was selected to enhance the cycling stability.

The cyclic voltammetry (CV) curves of LVP-G-FD in 2.5–4.2 V are shown in the Fig. 3a. In the first anodic scan, three oxidant peaks can be observed at 3.48, 3.61 and 4.10 V, corresponding to the extraction of two Li$^+$ ions from LVP. For the subsequent cathodic scan, four reduced peaks occurred at 3.05, 3.17, 3.55 and 3.63 V, respectively, which is different from the CV curves of LVP as LIBs cathode, indicating the insertion of Na$^+$ ions during the discharge process. In the second and third cycles, the oxidant peak located at 3.48 V and the reductant peaks located at 3.17 and 3.63 V gradually weakened and disappeared, and the peaks located at 3.61 and 4.10 V shifted to high potential, indicating the larger polarization due to the poor kinetics of Na$^+$ ions. In addition, similar results can be observed from the CV curves of LVP-G-D and LVP-FD (Fig. S9).

Galvanostatic discharge/charge measurements of the three samples

have also been carried out. At the low current density (20 mA g^{-1}), LVP-G-FD displays an initial discharge capacity of 101 mAh g^{-1}, which is similar with that of LVP-G-D (103 mAh g^{-1}) and higher than that of LVP-FD (86 mAh g^{-1}) (Fig. 3b). Moreover, LVP-G-FD displays an excellent cycling stability. After 50 cycles, LVP-G-FD maintains a discharge capacity of 99 mAh g^{-1}, corresponding to 98.0% of the initial discharge capacity, which is higher than those of LVP-G-D (83.5%) and LVP-FD (75.6%). The capacity of LVP-G-FD increases in the first several cycles, which may be ascribed to the graphene frameworks which lead to the slower infiltration of electrolyte and the infiltration continually happen in the first several cycles. The corresponding charge/discharge curves of the three samples are shown in Fig. 3c. Three plateaus can be observed at ~3.78, ~3.19 and ~3.16 V in the discharge curve of LVP-G-FD, respectively. The inconsistent overpotential between CV curves and charge/discharge curves may be attributed to the different polarization due to the different current density. Besides, the rate performance of the three samples has also been investigated (Fig. 3d). With the current density increasing, LVP-G-FD displays the smallest capacity decay among three samples. As the current density increased to 1000 mA g^{-1}, the discharge capacity of LVP-G-FD is as high as 66 mAh g^{-1}, which is higher than those of LVP-G-D (52 mAh g^{-1}) and LVP-FD (19 mAh g^{-1}). The enhanced cycling stability and rate performance of LVP-G-FD is attributed to the graphene framework, which provides void spaces to buffer the stress of ion insertion/extraction during the cycling and constructs efficient electronic conduction network [26–28]. The long-term cycling stability of LVP-G-FD was further investigated (Fig. 3e). At the current density of 500 mA g^{-1}, LVP-G-FD exhibits an initial capacity of 80 mAh g^{-1}. Moreover, no evident capacity decay can be observed in the first 100
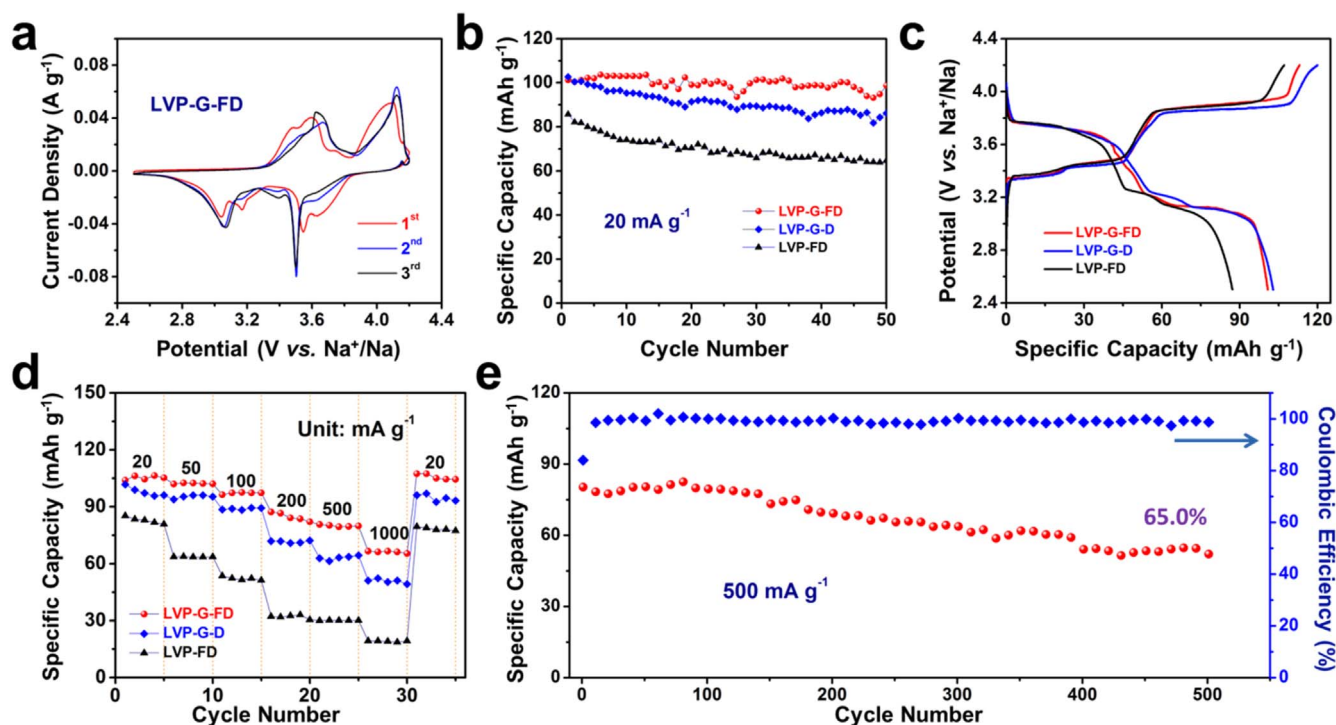
Fig. 3. The electrochemical performances of LVP in the potential range from 2.5 to 4.2 V: (a) The CV curves of LVP-G-FD in first three cycles at a scan rate of 0.1 mV s^{-1}. (b) The cycling stability and (c) charge/discharge curves of LVP-G-FD, LVP-G-D and LVP-FD at 20 mA g^{-1}. (d) The rate performance of LVP-G-FD, LVP-G-D and LVP-FD and (e) the cycling performance of LVP-G-FD at 500 mA g^{-1}. All the specific capacities are based on the mass of LVP. The potential window was expanded to 2.5–4.4 V at the current density of 500 and 1000 mA g^{-1}.
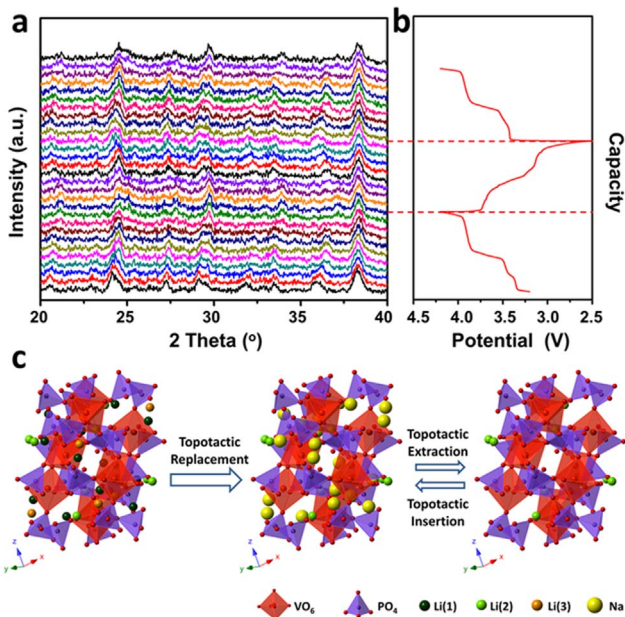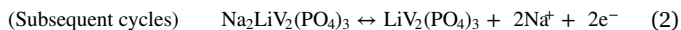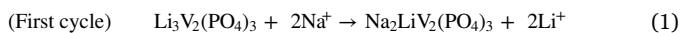

Fig. 4. (a) *In-situ* XRD patterns of LVP-G-FD during the first cycle and second charge process in potential window 2.5–4.2 V and (b) corresponding charge/discharge curves. (c) The schematic illustration of ions insertion/extraction mechanism for LVP as cathode for SIBs.

cycles. Besides, LVP-G-FD displays a capacity retention of 65.0% after 500 cycles. Also the Coulombic efficiency is approximately to 100% during the cycling except 84.1% in the first cycle. LVP-G-FD displays an excellent cycling stability after optimizing the potential range.

The ion insertion/extraction mechanism of LVP as cathode of SIBs has been investigated *via in-situ* XRD and ICP technology. Based on the ICP test, the molar ratio of Li, Na and V in the LVP-G-FD after soaking in the electrolyte for 12 h is 3.34: 0.30: 2.00. The existence of

Na element may be attributed to the adsorption of electrolyte on the surface of LVP-G-FD, indicating that the ion exchange is not obvious which is different from NVP as cathode for LIBs [22]. Fig. 4a shows the *in-situ* XRD patterns of the LVP-G-FD during the first cycle and second charge process in the potential range from 2.5 to 4.2 V, and the corresponding voltage curve is displayed in Fig. 4b. In the first charge process, the *in-situ* XRD patterns are corresponding well with that of LVP as cathode for LIBs, which has been considered as two-phase reaction [48]. In the subsequent discharge process, the change of *in-situ* XRD patterns can be considered as the inverse process of that in first charge process. Besides, the discharge plateaus correspond well with charge plateaus, indicating the reversible crystal structural change. Thus, sodium-ion storage of LVP in the first discharge process may also be two-phase reaction. Based on ICP result, the ratio of Li, Na and V in the LVP-G-FD after first cycle is 1.38: 1.53: 2.00, which corresponds well as lithium-ions extract at first charge process (initial charge capacity of 114 mAh g^{-1} corresponds to the extraction of about 1.73 lithium-ions per formula) and sodium-ions insert at the first discharge process (initial discharge capacity of 101 mAh g^{-1} corresponds to the insertion of about 1.53 sodium-ions per formula). Besides, the lattice parameters of LVP-G-FD after first charge/discharge process are larger than those of fresh LVP-G-FD (Table S1), which can be attributed to the larger ionic radius of sodium-ion (*vs.* lithium-ion). The first charge/discharge process in the potential range from 2.5 to 4.2 V is an electrochemical topotactic replacement process in which sodium-ions replace part lithium ions of LVP. Moreover, the *in-situ* XRD patterns of the subsequent charge process demonstrate the reversible change of crystal structure of LVP during the sodium-ion storage. Based on the above analysis, the theoretical ion insertion/extraction mechanism of LVP as SIBs cathode can be described as Fig. 4c and Eqs. (1) and (2). Firstly, electrochemical topotactic replacement process (sodium-ions replace part lithium ions of LVP) occurs in the first cycle. Then, the topotactic reaction (reversible insertion/extraction of Na$^+$ ions) occurs during the subsequent cycles.

(First cycle) $\quad Li_3V_2(PO_4)_3 + 2Na^+ \rightarrow Na_2LiV_2(PO_4)_3 + 2Li^+$ $\qquad$ (1)

(Subsequent cycles) $\quad Na_2LiV_2(PO_4)_3 \leftrightarrow LiV_2(PO_4)_3 + 2Na^+ + 2e^-$ $\qquad$ (2)

3. Conclusions

The reversible sodium-ion storage of LVP has been realized with electrochemical topotactic replacement and topotactic reaction, and the modified LVP has been evaluated as a promising cathode material for SIBs. The graphene framework wrapped LVP achieved a high energy density of 501.3 Wh kg^{-1}, which is higher than those of most poly-anionic compound cathodes for SIBs. Moreover, LVP-G-FD also displayed an excellent cycling stability that the capacity retention of 65.0% after 500 cycles was obtained. Our work demonstrates that LVP is a promising cathode material for high-energy density SIBs and our investigation on LVP as cathode for SIBs will inspire the future success in exploiting superior electrode materials for next-generation high-energy density SIBs.

4. Experimental section

4.1. Sample synthesis

$CH_3COOLi\cdot2H_2O$, V_2O_5, $H_2C_2O_4\cdot2H_2O$, and $NH_4H_2PO_4$, of analytical grade, were all purchased from the Sinopharm Chemical Reagent Co., Ltd. (Shanghai, China). In a typical synthesis, V_2O_5 (2 mmol) and $H_2C_2O_4\cdot2H_2O$ (6 mmol) were dissolved into deionized water (20 mL) and vigorously stirred at 70 °C for 1 h to obtain a blue VOC_2O_4 solution. Then $NH_4H_2PO_4$ (6 mmol) and $CH_3COOLi\cdot2H_2O$ (6 mmol) were added into the solution, which was further stirred for 5 min. After that, graphene oxide suspension (20 mL, 2 mg mL^{-1}, synthesized through a modified Hummer's method) was added into the solution and stirring was continued for more than 30 min. Then, the solution was frozen and then underwent a freeze-drying process to obtain the precursor and the precursor was manually grinded to powder. Finally, the graphene framework wrapped LVP (LVP-G-FD) were obtained from the precursor powder by preheating it at 400 °C for 4 h followed by annealing at 700 °C for 8 h in N_2 atmosphere with a heating rate of 5 °C min^{-1}. LVP-FD was obtained by changing the graphene oxide suspension to deionized water, and LVP-G-D was obtained by changing freeze-drying treatment to direct drying.

4.2. Structure characterization

XRD and in-situ XRD measurements were performed to investigate the crystallographic structure using a D8 Advance X-ray diffractometer with a nonmonochromated Cu Kα X-ray source. The FESEM images and EDS elemental mappings were collected with a JEOL-7100F microscope at an acceleration voltage of 20 kV. TEM and HRTEM images were recorded by using a JEM-2100F STEM/EDS microscope. BET surface areas were measured using a Tristar II 3020 instrument by adsorption of nitrogen at 77 K. Raman spectra were obtained using a Renishaw INVIA micro-Raman spectroscopy system. The carbon content analyses were performed by Elementar Vario EL cube elemental analyzer. ICP test were performed by PerkinElmer Optima 4300DV spectrometer.

4.3. Electrochemical measurements

The electrochemical properties were characterized by assembling 2016 coin cells in a glove box ($O_2\leq1$ ppm and $H_2O\leq1$ ppm), which used sodium pellet as anode and glass fiber as separator. The electrolyte is composed of 1 M $NaClO_4$ dissolved in EC (ethylene carbonate)/DMC (dimethyl carbonate) (volume ratio of 1:1) with 5 wt% FEC (fluor-oethylene carbonate). Cathodes were obtained with 60% as-synthesized active materials, 30% acetylene black and 10% poly(tetrafluoroethylene) (PTFE). The loading of the active material was about 6–8 mg cm^{-2}. Galvanostatic charge/discharge cycling behavior was investigated in a potential range of 2.5–4.5/2.5–4.2 V vs. Na^+/Na with a multichannel battery testing system (LAND CT2001A). CV curves were acquired with an electrochemical workstation (Autolab PGSTAT 302 and CHI 760D).

Appendix A. Supporting information

Supplementary data associated with this article can be found in the online version at doi:10.1016/j.nanoen.2016.12.050.

References

[1] Z. Yang, J. Zhang, M.C. Kintner-Meyer, X. Lu, D. Choi, J.P. Lemmon, J. Liu, Chem. Rev. 111 (2011) 3577–3613.
[2] Y. Liu, Y. Qiao, W. Zhang, Z. Li, X. Ji, L. Miao, L. Yuan, X. Hu, Y. Huang, Nano Energy 12 (2015) 386–393.
[3] H. Pan, Y.-S. Hu, L. Chen, Energy Environ. Sci. 6 (2013) 2338.
[4] N. Yabuuchi, K. Kubota, M. Dahbi, S. Komaba, Chem. Rev. 114 (2014) 11636–11682.
[5] X. Xiang, K. Zhang, J. Chen, Adv. Mater. 27 (2015) 5343–5364.
[6] W. Luo, F. Shen, C. Bommier, H. Zhu, X. Ji, L. Hu, Acc. Chem. Res. 49 (2016) 231–240.
[7] J. Ni, S. Fu, C. Wu, Y. Zhao, J. Maier, Y. Yu, L. Li, Adv. Energy Mater. 6 (2016) 1502568.
[8] S. Li, Y. Dong, L. Xu, X. Xu, L. He, L. Mai, Adv. Mater. 26 (2014) 3545–3553.
[9] D. Su, C. Wang, H. j. Ahn, G. Wang, Chem. Eur. J. 19 (2013) 10884–10889.
[10] P. Vassilaras, X. Ma, X. Li, G. Ceder, J. Electrochem. Soc. 160 (2013) A207–A211.
[11] J. Ding, Y. Zhou, Q. Sun, X. Yu, X. Yang, Z. Fu, Electrochim. Acta 87 (2013) 388–393.
[12] V. Raju, J. Rains, C. Gates, W. Luo, X. Wang, W.F. Stickle, G.D. Stucky, X. Ji, Nano Lett. 14 (2014) 4119–4124.
[13] Q. Wei, J. Liu, W. Feng, J. Sheng, X. Tian, L. He, Q. An, L. Mai, J. Mater. Chem. A 3 (2015) 8070–8075.
[14] Y. Li, D. Wang, Q. An, B. Ren, Y. Rong, Y. Yao, J. Mater. Chem. A 4 (2016) 5402–5405.
[15] C. Zhu, K. Song, P.A. van Aken, J. Maier, Y. Yu, Nano Lett. 14 (2014) 2175–2180.
[16] H. Kim, R. Shakoor, C. Park, S.Y. Lim, J.S. Kim, Y.N. Jo, W. Cho, K. Miyasaka, R. Kahraman, Y. Jung, Adv. Funct. Mater. 23 (2013) 1147–1155.
[17] P. Barpanda, T. Ye, M. Avdeev, S.-C. Chung, A. Yamada, J. Mater. Chem. A 1 (2013) 4194–4197.
[18] P. Barpanda, J. Lu, T. Ye, M. Kajiyama, S.-C. Chung, N. Yabuuchi, S. Komaba, A. Yamada, RSC Adv. 3 (2013) 3857–3860.
[19] P. Singh, K. Shiva, H. Celio, J.B. Goodenough, Energy Environ. Sci. 8 (2015) 3000–3005.
[20] Q. Wei, Q. An, D. Chen, L. Mai, S. Chen, Y. Zhao, K.M. Hercule, L. Xu, A. Minhas-Khan, Q. Zhang, Nano Lett. 14 (2014) 1042–1048.
[21] C. Masquelier, L. Croguennec, Chem. Rev. 113 (2013) 6552–6591.
[22] Q. An, F. Xiong, Q. Wei, J. Sheng, L. He, D. Ma, Y. Yao, L. Mai, Adv. Energy Mater. 5 (2015) 1401963.
[23] Y. Jiang, Z. Yang, W. Li, L. Zeng, F. Pan, M. Wang, X. Wei, G. Hu, L. Gu, Y. Yu, Adv. Energy Mater. 5 (2015) 1402104.
[24] Y. Fang, L. Xiao, X. Ai, Y. Cao, H. Yang, Adv. Mater. 27 (2015) 5895–5900.
[25] X. Rui, Q. Yan, M. Skyllas-Kazacos, T.M. Lim, J. Power Sources 258 (2014) 19–38.
[26] Z.-S. Wu, G. Zhou, L.-C. Yin, W. Ren, F. Li, H.-M. Cheng, Nano Energy 1 (2012) 107–131.
[27] C.-S. Li, Y. Sun, W.-H. Lai, J.-Z. Wang, S.-L. Chou, ACS Appl. Mater. Interfaces 8 (2016) 27710–27719.
[28] W. Xiang, Z.-G. Wu, E.-H. Wang, M.-Z. Chen, Y. Song, J.-B. Zhang, Y.-J. Zhong, S.-L. Chou, J.-H. Luo, X.-D. Guo, J. Power Sources 329 (2016) 94–103.
[29] Q. Li, N. Mahmood, J. Zhu, Y. Hou, S. Sun, Nano Today 9 (2014) 668–683.

[30] N. Mahmood, C. Zhang, H. Yin, Y. Hou, J. Mater. Chem. A 2 (2014) 15–32.
[31] W. Zhang, Y. Liu, C. Chen, Z. Li, Y. Huang, X. Hu, Small 11 (2015) 3822–3829.
[32] X. Tang, S.S. Jan, Y. Qian, H. Xia, J. Ni, S.V. Savilov, S.M. Aldoshin, Sci. Rep. 5 (2015) 11958.
[33] N. Zhang, X. Han, Y. Liu, X. Hu, Q. Zhao, J. Chen, Adv. Energy Mater. 5 (2015) 1401123.
[34] J. Song, M. Xu, L. Wang, J.B. Goodenough, Chem. Commun. 49 (2013) 5280–5282.
[35] P. Barpanda, G. Oyama, S.-i. Nishimura, S.-C. Chung, A. Yamada, Nat. Commun. 5 (2014) 4358.
[36] A. William III, Energy Environ. Sci. 8 (2015) 540–545.
[37] W. Shen, C. Wang, H. Liu, W. Yang, Chem. Eur. J. 19 (2013) 14712–14718.
[38] C. Li, X. Miao, W. Chu, P. Wu, D.G. Tong, J. Mater. Chem. A 3 (2015) 8265–8271.
[39] H. Kim, I. Park, D.-H. Seo, S. Lee, S.-W. Kim, W.J. Kwon, Y.-U. Park, C.S. Kim, S. Jeon, K. Kang, J. Am. Chem. Soc. 134 (2012) 10369–10372.
[40] M. Nose, H. Nakayama, K. Nobuhara, H. Yamaguchi, S. Nakanishi, H. Iba, J. Power Sources 234 (2013) 175–179.
[41] M. Nose, S. Shiotani, H. Nakayama, K. Nobuhara, S. Nakanishi, H. Iba, Electrochem. Commun. 34 (2013) 266–269.
[42] Y.-L. Ruan, K. Wang, S.-D. Song, X. Han, B.-W. Cheng, Electrochim. Acta 160 (2015) 330–336.
[43] Y. Kawabe, N. Yabuuchi, M. Kajiyama, N. Fukuhara, T. Inamasu, R. Okuyama, I. Nakai, S. Komaba, Electrochem. Commun. 13 (2011) 1225–1228.
[44] K. Kubota, K. Yokoh, N. Yabuuchi, S. Komaba, Electrochemistry 82 (2014) 909–911.
[45] R. Shakoor, D.-H. Seo, H. Kim, Y.-U. Park, J. Kim, S.-W. Kim, H. Gwon, S. Lee, K. Kang, J. Mater. Chem. 22 (2012) 20535–20541.
[46] Y.U. Park, D.H. Seo, H. Kim, J. Kim, S. Lee, B. Kim, K. Kang, Adv. Funct. Mater. 24 (2014) 4603–4614.
[47] B. Pei, Z. Jiang, W. Zhang, Z. Yang, A. Manthiram, J. Power Sources 239 (2013) 475–482.
[48] M. Morcrette, Electrochem. Solid-State Lett. 6 (2003) A80–A84.

Fangyu Xiong received his B.S. degree in Material Physics and Chemistry from Wuhan University of Technology in 2016. He is currently working toward the Ph.D. degree and his current research interests focuses on electrode materials for emerging energy storage devices.

Shuangshuang Tan received his B.S. degree in Material Science and Engineering from Wuhan University of Technology in 2016. He is currently working toward the Ph.D. degree and his current research focuses on the energy storage materials and devices.

Qiulong Wei received his Ph.D. degree from Wuhan University of Technology in 2016. Now, he is a postdoctoral fellow with Prof. Bruce Dunn at University of California Los Angeles. His current research involves the design and synthesis of novel nanomaterials for achieving both high energy density and power density electrochemical energy storage device, including the lithium-ion battery, sodium-ion battery and the hybrid capacitor.

Guobin Zhang received his B.S. degree in Inorganic Nonmetallic Materials Engineering from Inner Mongolia University of Science & Technology in 2014 and he is currently working toward the Ph.D. degree. His current research interests include nanomaterials for Li-ions batteries, supercapacitors, sodium batteries and *in-situ* characterization.
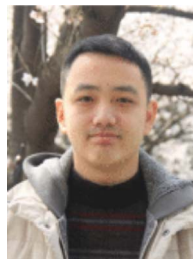
Jinzhi Sheng received his M.S. degree in Materials Engineering from Wuhan University of Technology in 2015. He is currently working toward the Ph.D. degree and his current research focuses on the energy storage materials and devices.
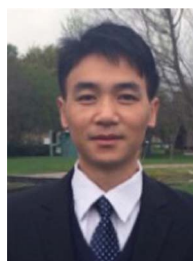
Qinyou An is Associate Professor of Materials Science and Engineering at Wuhan University of Technology (WUT). He received his Ph.D. degree from WUT in 2014. He carried out his postdoctoral research in the laboratory of Prof. Yan Yao at the University of Houston in 2014–2015. Currently, his research interest includes energy storage materials and devices.

Liqiang Mai is Chair Professor of Materials Science and Engineering at Wuhan University of Technology (WUT). He received his Ph.D. from WUT in 2004. He carried out his postdoctoral research in the laboratory of Prof. Zhonglin Wang at Georgia Institute of Technology in 2006–2007 and worked as advanced research scholar in the laboratory of Prof. Charles M. Lieber at Harvard University in 2008–2011. His current research interests focus on nanowire materials and devices for energy storage. He is the winner of the National Natural Science Fund for Distinguished Young Scholars, China Youth Science and Technology Award, and Guanghua Engineering Award, and so forth.